

# A symmetry-mode description of rigid-body rotations in crystalline solids: a case study of $\text{Mg}(\text{H}_2\text{O})_6\text{RbBr}_3$

Melanie Müller,<sup>a,b</sup> Robert E. Dinnebier,<sup>a</sup> Ann-Christin Dippel,<sup>c</sup> Harold T. Stokes<sup>d</sup> and Branton J. Campbell<sup>d\*</sup>

<sup>a</sup>Max Planck Institute for Solid State Research, Heisenbergstrasse 1, Stuttgart 70569, Germany,

<sup>b</sup>University of Trento, Trento 38123, Italy, <sup>c</sup>Deutsches Elektronen-Synchrotron DESY, Hamburg 22607, Germany, and <sup>d</sup>Department of Physics and Astronomy, Brigham Young University, Provo, UT 84602, USA. Correspondence e-mail: branton\_campbell@byu.edu

The application of rotational symmetry modes to quantitative rigid-body analysis is demonstrated for octahedral rotations in  $\text{Mg}(\text{H}_2\text{O})_6\text{RbBr}_3$ . Rigid-body rotations are treated as axial-vector order parameters and projected using group-theoretical methods. The high-temperature crystal structure of the  $\text{Mg}(\text{H}_2\text{O})_6\text{RbBr}_3$  double salt consists of a cubic perovskite-like corner-sharing network of  $\text{RbBr}_6$  octahedra with isolated  $\text{MgO}_6$  octahedra at the perovskite *A* sites. A phase transition occurs at 411 K upon cooling, whereupon the  $\text{MgO}_6$  octahedra experience a substantial rigid-body rotation, the  $\text{RbBr}_6$  octahedra are translated but not rotated, and both types of octahedra become slightly distorted. The  $\text{MgO}_6$  rotation has three orthogonal components associated with the  $X_5^-$ ,  $\Gamma_4^+$  and  $X_1^-$  irreducible representations of the parent  $Pm\bar{3}m$  space-group symmetry which, given the weakly first-order character of the transition, appear to be strongly coupled. Parametric and sequential refinements of the temperature-dependent structure were conducted using four model types: (1) traditional atomic *xyz* coordinates for each atom, (2) traditional rigid-body parameters, (3) purely displacive symmetry modes and (4) rigid-body rotational symmetry modes. We demonstrate that rigid-body rotational symmetry modes are an especially effective parameter set for the Rietveld characterization of phase transitions involving polyhedral rotations.

© 2014 International Union of Crystallography

## 1. Introduction

The definition of rigid collections of atoms is an essential means of reducing effective complexity in numerous inorganic, molecular and macromolecular compounds. Originally developed as a tool for single-crystal analysis (Scheringer, 1963), the rigid-body parameter set is particularly useful in Rietveld analyses (Dinnebier, 1999; Hazen & Finger, 1979), and is now available in several Rietveld refinement packages. The external orientation of the rigid body around the pivot point is typically defined using Euler angles in an orthonormal coordinate system that has been set by convention relative to basis vectors of the crystal lattice. Depending on the type of structure, there may or may not be an atom located at the pivot point. The internal rigid-body parameters, which can be either fixed or refined, locate each of the passenger atoms of the rigid body in terms of interatomic bond distances, bond angles and torsion angles.

If only one symmetry-unique parent atom is displaced by a rigid-body rotation, it is most convenient to refine the atomic coordinates of the rigid-body atom directly. However, the number of displacive parameters required to describe the rotation scales linearly with the number of passenger atoms, in

contrast to the number of rotational parameters needed which is independent of the internal complexity. For a complicated molecular or polyhedral collection of atoms, the rigid-body description will be much more economical, in the sense that there will be fewer large-valued parameters. Of course, when the internal rigid-body parameters are accounted for, the total number of structural parameters is the same for both displacive and rigid-body models. However, even when the rigid body is quite flexible, the rigid-body parameter set will still be easier to interpret when the external rotation angles are large.

Many crystal structures can be viewed as low-symmetry distortions of some higher-symmetry parent structure. The word distortion is used generally here to refer to any type of physical order parameter, such as an atomic displacement, magnetic moment, site-occupancy variation *etc.* We traditionally define separate parameters for each symmetry-unique atom (*e.g.* *xyz* coordinates) and observe that the total number of free parameters is much greater in the distorted phase than in the parent. Alternatively, one can always use the irreducible representations (irreps) of the parent symmetry group to define a symmetry-motivated parameter set that spans the same space of achievable distortions and contains the same

number of parameters. These ‘symmetry modes’ are defined at specific points in reciprocal space (*i.e.* where corresponding superlattice intensities are observed) and consist of mutually orthogonal linear combinations of the traditional parameters. Furthermore, symmetry modes have zero amplitude in the parent structure, so that they effectively quantify deviations from the parent.

Because the symmetry-mode parameter set naturally lends itself to an invariant series expansion of the free energy, real phase transitions typically activate a relatively small fraction of the available modes. This reduction in the number of active (*i.e.* substantially nonzero) parameters can simplify a structure solution and stabilize a difficult structure refinement (Campbell *et al.*, 2007). Kerman *et al.* (2012) showed that for room-temperature  $\text{WO}_3$ , which exhibits a  $2 \times 2 \times 2$  supercell with 96 displacive modes in  $P1$  symmetry, only five substantially active independent modes arise. By independently identifying each of these modes, they were able to directly detect the correct space-group symmetry,  $P2_1/n$ , and to solve the distorted structure. Much recent work has successfully used displacive symmetry modes to describe distortions involving polyhedral tilt patterns (Swainson & Yonkeu, 2007; Howard *et al.*, 2008; Hatt & Spaldin, 2010; Lister *et al.*, 2010; Swainson *et al.*, 2010; Wang & Angel, 2011; Zhao *et al.*, 2011; Ati *et al.*, 2011; Peel *et al.*, 2012; Senn *et al.*, 2012; Yamauchi, 2013).

The development of a symmetry-adapted parameter set for rotations would provide a novel and potentially more effective means of characterizing phase transitions in rigid-body systems. Müller *et al.* (2010) conducted a parametric rigid-body refinement of the temperature-dependent structure of  $\text{CeFeO}_2$ , which undergoes a phase transition upon cooling ( $Fm\bar{3}m \rightarrow Pbcn$ ) at 353 K, wherein the corner-sharing  $\text{FeO}_4$  tetrahedra experience significant reorientation. They also performed a parametric refinement of displacive symmetry-mode parameters for comparison. Because the  $\text{FeO}_4$  tetrahedra are structurally very simple, both parameter sets were effective. However, for more complicated rigid-body structures, it would be very helpful to combine the use of rigid bodies and symmetry modes. In the present work, we demonstrate just such a parameter set and describe the principles upon which it can be obtained. The internal parameters of a distorted rigid body could also be symmetry adapted using the irreps of the point group of the undistorted rigid body, but we focus on rotational symmetry modes here.

Displacive and rotational order parameters can be used to describe the same structure, but have very different tensor properties. An atomic displacement  $\mathbf{d}$  is a polar vector, meaning that, for any symmetry operation  $g$  contained in space group  $G$ , the symmetry-equivalent displacement will be  $g(\mathbf{d}) = S_g \cdot \mathbf{d}$ , where  $S_g$  is the three-dimensional matrix operator associated with  $g$ . In contrast, a rotation vector  $\mathbf{r}$  is an axial vector (also known as a pseudo-vector), which means that  $g(\mathbf{r}) = \text{Det}(S_g)S_g \cdot \mathbf{r}$ , where the determinant equals +1 for proper symmetry operations (*e.g.* rotations and translations) and  $-1$  for improper symmetry operations (*e.g.* reflections and inversions). Using the implementation of axial vectors in the *ISOTROPY* program, Howard & Stokes (1998, 2005)

employed axial-vector order parameters to qualitatively describe octahedral tilt patterns in distorted perovskites. Rotational symmetry modes have also been examined for spinel structures (Talanov & Shirokov, 2012). These order parameters were all defined using the crystallographic space groups published in Volume A of *International Tables for Crystallography* (Hahn, 1983).

$\text{Mg}(\text{H}_2\text{O})_6\text{RbBr}_3$  was selected for the present case study because of the presence of two chemically distinct rigid polyhedral units and a conveniently accessible phase transition that gives rise to an interesting pattern of large-angle rigid-body rotations. The crystal structure of  $\text{Mg}(\text{H}_2\text{O})_6\text{RbBr}_3$  at room temperature (referred to here as the low-temperature or LT structure) was first described by Dinnebier *et al.* (2008) and found to be isostructural to other magnesium double salts, *e.g.*  $\text{Mg}(\text{H}_2\text{O})_6\text{RbCl}_3$  (Marsh, 1992) or  $\text{Mg}(\text{H}_2\text{O})_6(\text{NH}_4)\text{Cl}_3$  (Solans *et al.*, 1983). It has monoclinic  $C2/c$  symmetry, though its metric is nearly orthorhombic:  $a = 9.645$  (3),  $b = 9.868$  (3),  $c = 13.791$  (5) Å and  $\beta = 90.07$  (1)°, as illustrated on the left-hand panel of Fig. 1. Its structure is characterized by a three-dimensional network of corner-sharing  $\text{RbBr}_6$  octahedra that contains one  $\text{Mg}(\text{OH}_2)_6$  octahedron in the center of each void. If each  $\text{Mg}(\text{OH}_2)_6$  unit were replaced by an atom  $X$ , located at the center of gravity, the resulting  $X\text{RbBr}_3$  structure would be analogous to a  $2^{1/2} \times 2^{1/2} \times 2$  supercell of a distorted cubic perovskite with  $a = 6.94189$  Å, and with Rb on the  $B$  site and  $X$  on the  $A$  site. The octahedral rigid bodies employed are illustrated in Fig. 2.

At elevated temperatures,  $\text{Mg}(\text{H}_2\text{O})_6\text{RbBr}_3$  undergoes a reversible phase transition to a cubic ( $Pm\bar{3}m$ ) high-temperature (HT) structure analogous to an ideal perovskite. In an

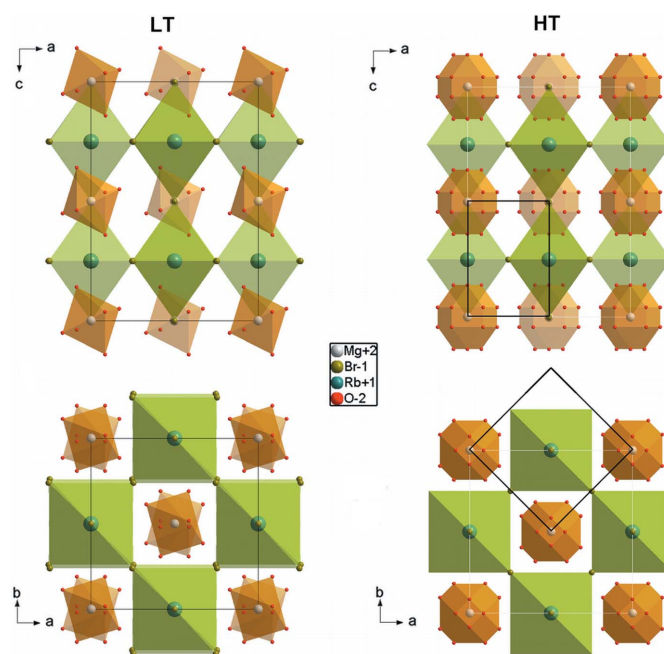


**Figure 1**  
Comparison of the LT (left view) and HT (right view) crystal structures of  $\text{Mg}(\text{H}_2\text{O})_6\text{RbBr}_3$  as viewed along the  $b$  axis (top panel) and the  $c$  axis (bottom panel). In the panels of the HT phase, the new cubic unit cell is indicated in black.

open system, the phase transition occurs at approximately  $T = 358$  K (Dinnebier *et al.*, 2008), while in a closed system, it is shifted to a considerably higher temperature of  $T = 408$  K (Emons *et al.*, 1991). The HT structure exhibits fourfold orientational disorder of its  $\text{Mg}(\text{OH}_2)_6$  octahedral tilts as illustrated in the right-hand panel of Fig. 1 (Dinnebier *et al.*, 2008), which then grow in size and become orientationally ordered in the LT phase, so that the tilts alternate along the long axis of the supercell. The  $\text{RbBr}_6$  octahedra remain untilted above and below the transition. Note that our symmetry-mode description of the LT phase is referenced to an idealized cubic parent structure in which the  $\text{Mg}(\text{OH}_2)_6$  octahedra are ordered and aligned parallel to the cell axes (see Fig. 3), though the actual HT structure is orientationally disordered.

## 2. Methods

The synthesis of  $\text{Mg}(\text{H}_2\text{O})_6\text{RbBr}_3$  was performed as stated by Dinnebier *et al.* (2008). The compound was obtained from

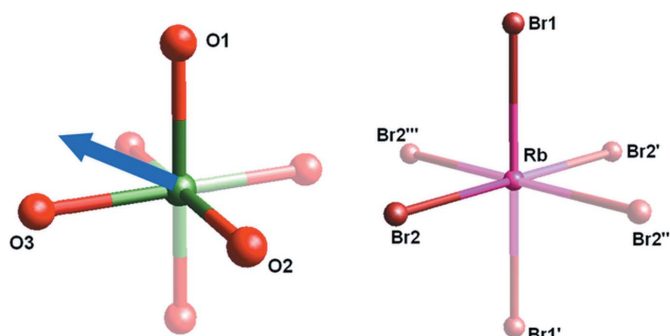


**Figure 2**  
 $\text{MgO}_6$  (left view) and  $\text{RbBr}_3$  (right view) octahedral rigid bodies of  $\text{Mg}(\text{H}_2\text{O})_6\text{RbBr}_3$  used for the refinement of the RB and DM models. The solid atoms are defined explicitly, whereas the semitransparent atoms are generated *via* space-group symmetry. The blue vector indicates the general rotation axis of the  $\text{MgO}_6$  octahedron, which is the sum of three vector components in the RM model.

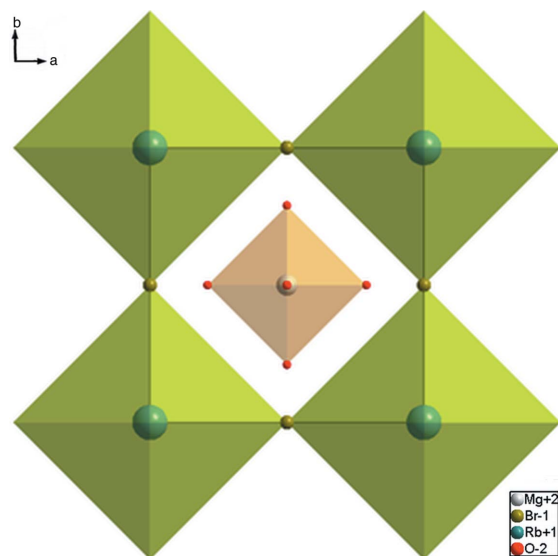


**Figure 3**  
 Idealized cubic parent structure of  $\text{Mg}(\text{H}_2\text{O})_6\text{RbBr}_3$ , in which the high-temperature orientation disorder has been eliminated.

slow isothermal crystallization from an aqueous solution containing 82.68 mg of  $\text{RbBr}$  and 92.05 mg of  $\text{MgBr}_2$  at 323 K.

High-resolution laboratory X-ray powder diffraction data (Fig. 4) were recorded using a Bruker D8 diffractometer in Debye–Scherrer geometry, equipped with a Vantec-1 position-sensitive detector ( $6^\circ$  opening angle) and  $\text{Cu } K\alpha_1$  radiation ( $1.540596 \text{ \AA}$ ) obtained from a primary  $\text{Ge}(111)$  Johansson monochromator. The sample was sealed in a glass capillary and rotated during the measurement in order to improve the orientational uniformity of the powder. The instrumental profile was determined from a measurement of the NIST SRM 660a  $\text{LaB}_6$  standard.

Furthermore, *in situ* temperature-dependent powder diffraction data were collected at the high-energy powder diffraction beamline P02.1 of the Petra III synchrotron using a wavelength of  $0.20752 \text{ \AA}$ . The sample was sealed in a glass capillary and measurements were performed in the temperature range from 303 to 422 K with a constant heating rate of  $2 \text{ K min}^{-1}$ . The exposure time was two minutes for each data set. A two-dimensional simulated Guinier plot, prepared with the *Powder 3D* software (Hinrichsen *et al.*, 2006), is shown in Fig. 5. In this plot, the observed intensity is plotted *versus* diffraction angle  $2\theta$  and temperature  $T$ . The phase transition is easily recognized from the merging of several groups of diffraction peaks as the high-symmetry phase is realized; this occurs at about set number 37, which corresponds to 411 K. At about 420 K, a dehydrated phase appears as a decomposition product, which will not be discussed further in the present work.

Rietveld refinements were performed using the *TOPAS* software (version 4.2; Bruker AXS GmbH, Karlsruhe, Germany). In each refinement, the background was modeled using a Chebyshev polynomial. The instrumental broadening was implemented by the fundamental parameter approach of Cheary & Coelho (1992) as available in *TOPAS*. In addition to  $\text{Mg}(\text{H}_2\text{O})_6\text{RbBr}_3$ , a small amount (about 3.5 wt%) of  $\text{RbBr}$  is present in the sample and was therefore included in the

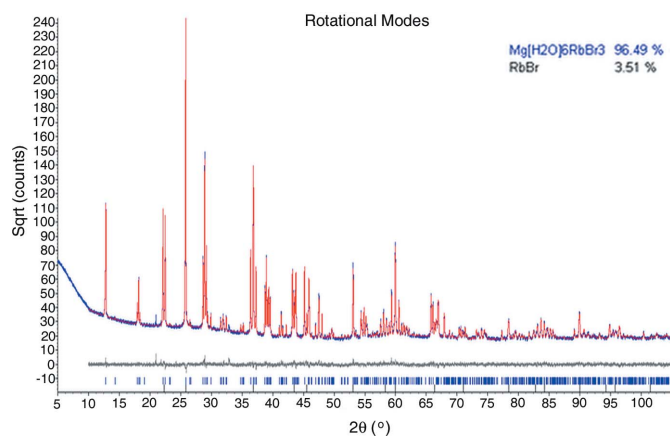


**Figure 4**  
 Rietveld fit of the RM model of  $\text{Mg}(\text{H}_2\text{O})_6\text{RbBr}_3$  against room-temperature laboratory powder diffraction data. The red and blue lines correspond to the calculated and measured patterns, respectively. The difference (measured minus calculated) pattern is indicated by the grey line. All four models resulted in comparable fits.

refinements as a second phase. To make the definition of rigid bodies more convenient in *TOPAS*, we added zero-occupancy hydrogen atoms to the model as needed. When using rotational symmetry modes, a dummy hydrogen atom was placed within each rigid body to define the rotation axis relative to the center of rotation.

### 3. Results and discussion

The  $C2/m$  space-group symmetry of  $\text{Mg}(\text{H}_2\text{O})_6\text{RbBr}_3$  permits 13 displacive degrees of freedom (DOFs) in the LT structure:  $\text{O1}(x, y, z)$ ,  $\text{O2}(x, y, z)$ ,  $\text{O3}(x, y, z)$ ,  $\text{Br2}(x, y, z)$ ,  $\text{Rb}(y)$ . Though the oxygen atoms are located on general positions, the  $\text{MgO}_6$  octahedron lies on an inversion center, so that opposite pairs of oxygen atoms are related by symmetry. The three oxygen-atom displacements contribute to three substantial rotational DOFs and six small internal DOFs. The  $\text{RbBr}_6$  octahedron is centered on a twofold axis, which is capable of supporting extended-body rotations about the  $y$  axis. Though the Br2 atom lies on a general position, it joins two adjacent octahedra separated by a C-centering translation, which must rotate in the same direction. Because such a rotation would split each Br2 atom in half, and is therefore topologically impossible, the Br2 displacement contributes three internal rigid-body DOFs but no rotational DOFs. The Rb atoms lie on twofold axes and can therefore be displaced along  $y$  and followed by the Br2 atoms. However, this octahedral translation must be tightly coupled to the internal rigid-body DOFs since the Br1 atoms lie on inversion centers, which cannot be displaced. All structural DOFs associated with  $\text{RbBr}_6$  proved to be quite small.

Using the *ISODISTORT* software package (Campbell *et al.*, 2006), we find that the pattern of atomic displacements in  $\text{Mg}(\text{H}_2\text{O})_6\text{RbBr}_3$  can also be described using 13 displacive symmetry modes. These symmetry modes belong to seven different irreps of the parent cubic symmetry group:  $\Gamma_1^+$ ,  $\Gamma_3^+$ ,  $\Gamma_4^+$ ,  $\Gamma_5^+$ ,  $X_1^-$ ,  $X_4^-$ ,  $X_5^-$ . The  $\Gamma$  point is located at  $k = (0, 0, 0)$  in

the first Brillouin zone of the reciprocal lattice, while the  $X$  point is located at  $k = (0, \frac{1}{2}, 0)$ , where superlattice intensity is observed. For the  $\text{MgO}_6$  octahedra,  $X_5^-$ ,  $\Gamma_4^+$  and  $X_1^-$  provide three rotations about the respective  $x$ ,  $y$  and  $z$  axes, while  $\Gamma_1^+$ ,  $\Gamma_3^+$ ,  $2\Gamma_5^+$ ,  $X_4^-$  and  $X_5^-$  give rise to six internal modes.  $\Gamma_1^+$ , for example, is responsible for the isotropic breathing mode of  $\text{MgO}_6$ , which is also available in the parent cubic structure. For the  $\text{RbBr}_6$  octahedra,  $X_5^-$  yields one translation along  $y$ , while  $X_4^-$  and  $2X_5^-$  give rise to three internal modes.

*ISODISTORT* was also used to calculate rotational (*i.e.* axial vector) symmetry modes, where irreps  $X_5^-$ ,  $\Gamma_4^+$  and  $X_1^-$  yield the respective  $x$ ,  $y$  and  $z$  components of the rotation vector of  $\text{MgO}_6$ . In addition,  $\Gamma_4^+$  generates a topologically impossible (but not symmetry forbidden)  $\text{RbBr}_6$  rotation about the  $y$  axis, which cannot be refined. Because *ISODISTORT* has not yet implemented the projection of axial-vector order parameters from parent structures with crystallographic space-group symmetry, we used the more complicated but entirely equivalent procedure of projecting magnetic moment vectors (also axial vectors) from a paramagnetic parent to obtain a magnetic structure with a type-1 magnetic space group (*i.e.* Fedorov group), and then simply reinterpreted each magnetic moment vector (measured in  $\mu_B$ ) as a rotation angle (measured in radians).

For the structural description of  $\text{Mg}(\text{H}_2\text{O})_6\text{RbBr}_3$ , four different models were used in Rietveld refinements against X-ray powder diffraction data:

(1) The atomic coordinate (AC) model provides 13 free atomic coordinates as independent parameters.

(2) The displacive symmetry-mode (DM) model provides 13 displacive symmetry modes.

(3) The rigid-body (RB) model provides three orientation angles for the  $\text{MgO}_6$  octahedra, one translation mode for the  $\text{RbBr}_6$  octahedra, and nine Z-matrix parameters for the internal rigid-body DOFs.

(4) The rotational symmetry-mode (RM) model provides three rotational symmetry modes for the orientation of the  $\text{MgO}_6$  octahedra, one  $X_5^-$  translation mode for the  $\text{RbBr}_6$  octahedra and nine Z-matrix parameters for the internal rigid-body DOFs.

A comparison of the room-temperature lattice parameters and fractional atomic coordinates further showed that, for a given parameter, the fitted values obtained from the various models fall within two standard uncertainties (s.u.'s) of one another. The calculated  $R$  value ( $R_p$ ) also indicates that all four models yielded comparable results:  $R_p = 4.14\%$  for AC,  $R_p = 4.16\%$  for RB,  $R_p = 4.24\%$  for DM,  $R_p = 4.17\%$  for DM and for all cases  $R_{\text{exp}} = 3.66\%$ .

Sequential and parametric (Stinton & Evans, 2007) Rietveld refinements of the temperature-dependent *in situ* synchrotron powder diffraction data of  $\text{Mg}(\text{H}_2\text{O})_6\text{RbBr}_3$  were performed using all four structural models (AC, RB, DM, RM).<sup>1</sup>

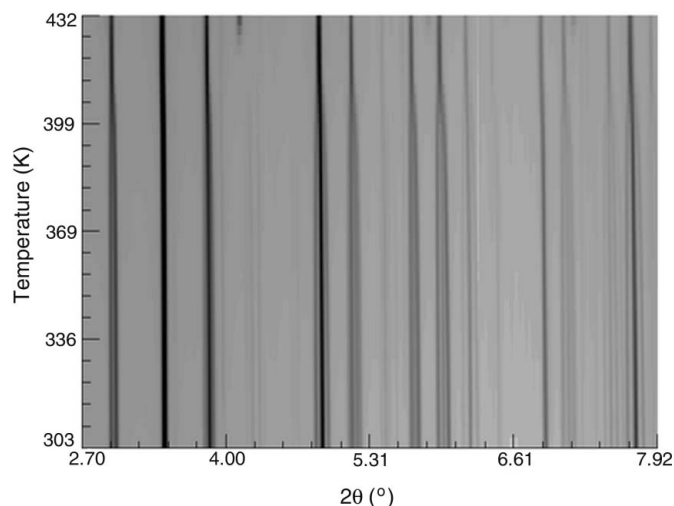


**Figure 5**

Simulated two-dimensional temperature-dependent Guinier plot of  $\text{Mg}(\text{H}_2\text{O})_6\text{RbBr}_3$ . The cubic monoclinic phase transition can be seen as several groups of peaks join at approximately 411 K. At about 418 K, a first-order phase transition occurs, whereupon the sample begins to dehydrate.

<sup>1</sup> The *TOPAS* input for the room-temperature fits of each model is included in the supporting information available from the IUCr electronic archives (Reference: TO5065).

Unlike the traditional AC model, the RB, DM and RM models all provide natural and/or intuitive structural constraints (*i.e.* internal rigid-body parameter deviations or displacive symmetry-mode amplitudes that are clearly insubstantial and can therefore be fixed), effectively reducing the structural complexity and stabilizing the refinement. In both the RB and RM models, the three internal angles of  $\text{MgO}_6$  were judged to be insubstantial and fixed to  $90^\circ$ . The inter-atomic distances of the  $\text{RbBr}_6$  rigid body need to be constrained to the lattice parameter, and its  $y$ -axis translation was proven to be indistinguishable from zero. This reduced the total number of DOFs to seven. In the DM model, only seven of the 13 displacive symmetry modes were judged to be active as they provide the same possibilities for atomic movement as the RB and RM approaches. Some modes (*e.g.* the two  $X_5^-$  modes for oxygen) need to be coupled in order to preserve the shape of the  $\text{MgO}_6$  octahedron. The non-active modes distort the octahedra either in angle or by variation of bond lengths and are therefore neglected.

For each of the four methods, sequential Rietveld refinements showed that the variable structural parameters exhibit a typical power law behavior. For this reason, the free parameters of the LT phase were assumed to follow a temperature trend of the form  $Q = f|T_{\text{crit}} - T|^{\beta^*}$ , where  $T_{\text{crit}}$  is the transi-

tion temperature,  $f$  quantifies the amplitude of the variation and  $\beta^*$  is a critical exponent. Because this phase transition involves the superposition of multiple order parameters, it must be first order, though it is only weakly first order, showing no obvious discontinuities at  $T_{\text{crit}}$ . However, even for a weakly first-order transition, the fluctuations do not normally become critical, so that it is not easy to assign physical meaning to the exponents  $\beta^*$ . Thus we prefer to refer to ‘pseudo-critical’ exponents in this case.

The greater simplicity of the more constrained models (RB, DM, RM) clearly improved the stability of the parametric fits without sacrificing quality of fit, as seen in Fig. 6. For the sequential fits, however, all four models resulted in similar fits, proving the applicability of the different models. Using AC, the overall sequential refinement series is of sufficient quality, though the trends of the individual parameters are not unambiguous as some parameters are highly correlated. In the parametric Rietveld refinement, some trends of atomic positions are therefore difficult to model and lead to an unsatisfying fit. Using the DM description, out of 13 possible displacive modes, seven were refined, yielding sequential and parametric refinements of good quality. Considerable care was exercised in the choice of the starting parameters, especially in the parametric refinement, as the fit result and quality proved to be strongly dependent upon them. Furthermore, a careful investigation of possible mode coupling is necessary in order to preserve the structure. The RB and RM approaches yielded fit results comparable to those obtained from DM. In these cases, the oxygen atoms are constrained by rigid bodies, which stabilize the refinements and facilitate the refinement process as small variations in parameters are compensated so that the global minimum of the refinement is more easily reached. The interpretation and understanding of the atomic movements is easier. The three rigid-body rotational symmetry-mode amplitudes of  $\text{MgO}_6$  from the RM model, for both sequential and parametric fits, are shown in Fig. 7.

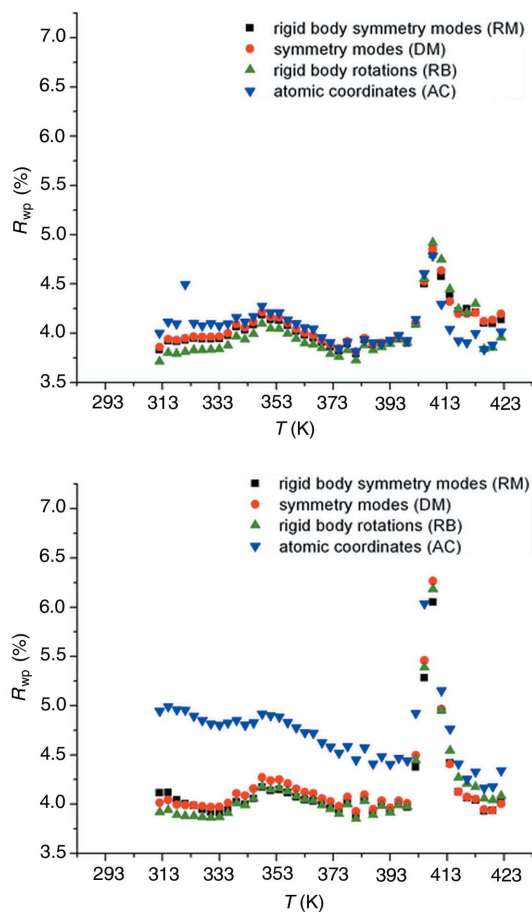


**Figure 6**  
 $R_{\text{wp}}$  values as obtained from sequential (top) and parametric (bottom) Rietveld refinements of  $\text{Mg}(\text{H}_2\text{O})_6\text{RbBr}_3$  using four different methods to describe the crystal structure.

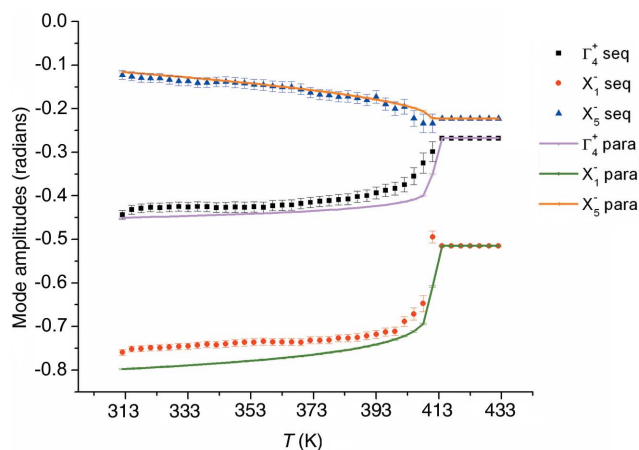


**Figure 7**  
Values obtained in sequential and parametric Rietveld refinement of the temperature-dependent synchrotron powder diffraction data for the three refined rigid-body rotational symmetry modes of the RM model. Those values are used to calculate the orientations of the rigid  $\text{MgO}_6$  octahedra.

It is important to note that both the RB and RM approaches can employ pure rotations with arbitrarily large angles, whereas the DM approach merely approximates pure rotations in the small-angle limit. Unlike the RB model, where the three orientation angles are applied sequentially, the three rotational symmetry modes (in radian units) in the RM model form the components (along the unit-cell axes) of a single rotation vector, which then determines the orientation of the octahedron and the positions of its passenger atoms; while the zero point of an RB-model angle is arbitrary, the zero point of an RM-model angle is strictly defined to correspond to the unrotated rigid body. Though the RB and RM approaches yielded comparable fits, the relative s.u.'s of the refined parameters obtained from the RM approach were smaller than those of the RB approach on average.

The behaviors of the lattice parameters and angles are independent of the atomic displacement model. Figs. 8 and 9 show their temperature dependencies in sequential and parametric refinements. Close to the refined transition temperature of  $T_{\text{crit}} = 411.08(2)$  K, the sequential refinement of the monoclinic  $\beta$  angle turned out to be unreliable because of its proximity to  $90^\circ$ . The pseudo-critical exponents obtained from the parametric refinement are  $\beta^* = 0.5$  for all cell edge lengths and  $\beta^* = 0.25$  for the monoclinic angle. The pseudo-critical exponents for the three  $\text{MgO}_6$  rotational symmetry modes of the RM model are determined to be  $\beta^* = 0.5$  for  $X_5^-$ ,  $\beta^* = 0.2$  for  $\Gamma_4^+$  and  $\beta^* = 0.25$  for  $X_1^-$ . Roughly the same values are obtained for the three angles of the RB model, as one might expect. We did not attempt to compare the values of the pseudo-critical exponents of orientational/displacive parameters across the four different models because the parameter sets are so different.

Typical values of  $\beta^*$  are one-half for ordinary scalar second-order transitions or one-quarter for a transition at the tricritical point that marks the boundary between first- and second-order transitions (Salje, 1990). While it is more difficult to interpret the exponents of a weakly first-order transition, the

$\beta^* = 0.5$  cell-parameter exponents do suggest a linear-quadratic coupling of the lattice strains to the large  $\text{MgO}_6$  rotation.

The cell parameters in Fig. 9 are derived from the cubic parent cell in the HT phase, but indicate a pseudo-orthorhombic strain in the LT phase. The rotational symmetry-mode amplitudes of the  $\text{MgO}_6$  octahedra (Fig. 7) have nonzero values even in the HT phase because the cubic average structure consists of orientationally disordered local octahedral rotations. Then, in the LT phase, the octahedral rotations become orientationally ordered, and the magnitudes of the two strongest rotational mode amplitudes also grow considerably. In order to accommodate nonzero rotations in the HT phase, we averaged the ordered superstructure over all of the symmetries of the parent structure, which superposed all possible local orientations of the  $\text{MgO}_6$  octahedra.

#### 4. Conclusions

The direct refinement of rigid-body rotational (axial-vector) symmetry modes across the cubic to monoclinic phase transition of  $\text{Mg}(\text{H}_2\text{O})_6\text{RbBr}_3$ , using both sequential and parametric refinement methods, was demonstrated using readily available structural analysis software. This novel parameter set (RM) was compared against a traditional but unconstrained atomic coordinate model (AC), a traditional rigid-body model (RB) and a purely displacive symmetry-mode model (DM). At a given temperature, all four models span the same atomic configuration space and, therefore, yield comparable fits as expected. Because the RB, DM and RM models each lend themselves to a unique set of natural or intuitive constraints, we employed those constraints to cut the number of refined parameters roughly in half, which resulted in significantly smaller s.u.'s compared to the AC model. The parametric fits of the three naturally constrained models were also substantially better than that of the AC model. Owing to the reduced number of parameters for the RB, DM and RM models, correlations are minimized, leading to more precise trends for

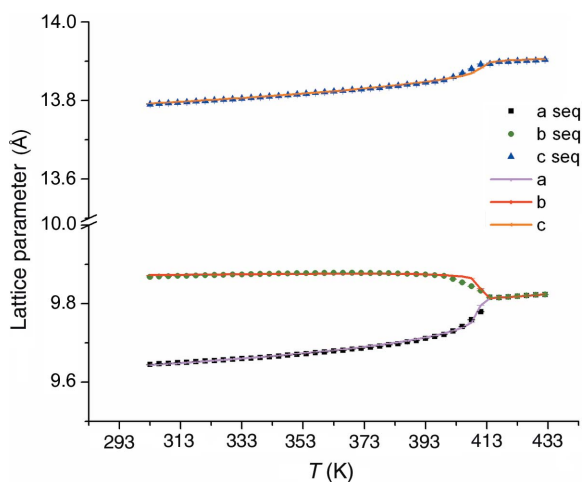


**Figure 8**  
Values for lattice parameters  $a$ ,  $b$  and  $c$  of  $\text{Mg}(\text{H}_2\text{O})_6\text{RbBr}_3$  obtained in sequential and parametric Rietveld refinements of the temperature-dependent synchrotron powder diffraction data.

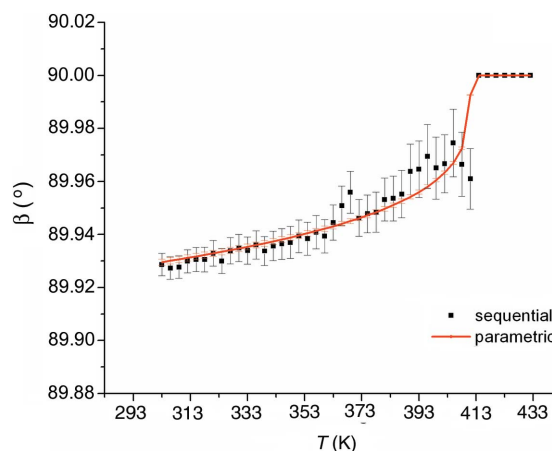


**Figure 9**  
Values obtained in sequential and parametric Rietveld refinement for monoclinic angle  $\beta$  from synchrotron powder diffraction data of  $\text{Mg}(\text{H}_2\text{O})_6\text{RbBr}_3$  as a function of temperature. Close to the transition temperature, the values obtained are not reliable because of large correlations.

each parameter, which simplifies the determination of suitable starting values for parametric models as well as their refinement.

Because this case study focused on a very simple octahedral rotation pattern, the RM model was no more effective than the RB or DM models. However, for highly complex structures involving polyhedral or molecular rigid-body motion, we anticipate that the natural constraints provided by rigid-body rotational symmetry modes (*i.e.* the RM model) will provide a much greater degree of structural simplification because of the preferential activation of modes belonging to a relatively small number of irreps.

We emphasize that our use of magnetic order parameters and a paramagnetic parent group was merely a convenient workaround, made possible by the fact that the resulting type-1 magnetic space group is isomorphic to the correct nonmagnetic space group. Axial-vector rotations can also be projected directly using nonmagnetic space groups, and we anticipate that the ISODISTORT software will have this capability in the future.

BJC would like to acknowledge helpful discussions with Ian Swainson and Simon Parsons. RED and MM acknowledge Frank Adams, Oksana Magdysyuk and Tomce Runcevski for data collection of the synchrotron powder diffraction pattern.

### References

- Ati, M., Melot, B., Chotard, J., Rousse, G., Reynaud, M. & Tarascon, J. (2011). *Electrochem. Commun.* **13**, 1280–1283.
- Campbell, B. J., Evans, J. S. O., Perselli, F. & Stokes, H. T. (2007). *IUCr Comput. Commun. Newsl.* **8**, 81–95.
- Campbell, B. J., Stokes, H. T., Tanner, D. E. & Hatch, D. M. (2006). *J. Appl. Cryst.* **39**, 607–614.
- Cheary, R. W. & Coelho, A. (1992). *J. Appl. Cryst.* **25**, 109–121.
- Dinnebier, R. E. (1999). *Powder Diffr.* **14**, 84–92.
- Dinnebier, R. E., Liebold-Ribeiro, Y. & Jansen, M. (2008). *Z. Anorg. Allg. Chem.* **634**, 1857–1862.
- Emons, H.-H., Voigt, H., Pohl, T. & Naumann, R. (1991). *J. Therm. Anal. Cal.* **37**, 1605–1691.
- Hatt, A. J. & Spaldin, N. A. (2010). *Phys. Rev. B*, **82**, 195402.
- Hazen, R. M. & Finger, L. W. (1979). *Phase Transitions*, **1**, 1–22.
- Hinrichsen, B., Dinnebier, R. E. & Jansen, M. (2006). *Z. Kristallogr. Suppl.* **23**, 231–236.
- Howard, C. J. & Stokes, H. T. (1998). *Acta Cryst.* **B54**, 782–789.
- Howard, C. J. & Stokes, H. T. (2005). *Acta Cryst.* **A61**, 93–111.
- Howard, C. J., Withers, R. L., Knight, K. S. & Zhang, Z. (2008). *J. Phys. Condens. Mater.* **20**, 135202.
- International Tables for Crystallography* (1983). Vol. A, edited by Th. Hahn. Dordrecht: Reidel.
- Kerman, S., Campbell, B. J., Satyavarapu, K. K., Stokes, H. T., Perselli, F. & Evans, J. S. O. (2012). *Acta Cryst.* **A68**, 222–234.
- Lister, S. E., Rixom, V. J. & Evans, J. S. O. (2010). *Chem. Mater.* **22**, 5279–5289.
- Marsh, R. E. (1992). *Acta Cryst.* **C48**, 218–219.
- Müller, M., Dinnebier, R. E., Ali, N. Z., Campbell, B. J. & Jansen, M. (2010). *Mater. Sci. Forum*, **651**, 79–95.
- Peel, M. D., Thompson, S. P., Daoud-Aladine, A., Ashbrook, S. E. & Lightfoot, P. (2012). *Inorg. Chem.* **51**, 6876–6889.
- Salje, E. K. H. (1990). *Phase Transitions in Ferroelastic and Co-elastic Crystals*. Cambridge University Press.
- Scheringer, C. (1963). *Acta Cryst.* **16**, 546–550.
- Senn, M. S., Wright, J. P. & Attfield, P. (2012). *Nature*, **481**, 173–176.
- Solans, X., Font-Altaba, M., Aguiló, M., Solans, J. & Domenech, V. (1983). *Acta Cryst.* **C39**, 1488–1490.
- Stinton, G. W. & Evans, J. S. O. (2007). *J. Appl. Cryst.* **40**, 87–95.
- Swainson, I., Chi, L., Her, J.-H., Cranswick, L., Stephens, P., Winkler, B., Wilson, D. J. & Milman, V. (2010). *Acta Cryst.* **B66**, 422–429.
- Swainson, I. P. & Yonkeu, A. L. (2007). *Am. Mineral.* **92**, 748–752.
- Talanov, V. M. & Shirokov, V. B. (2012). *Acta Cryst.* **A68**, 595–606.
- Wang, D. & Angel, R. J. (2011). *Acta Cryst.* **B67**, 302–314.
- Yamauchi, K. (2013). *J. Phys. Soc. Jpn.* **82**, 043702.
- Zhao, J., Ross, N. L., Wang, D. & Angel, R. J. (2011). *J. Phys. Condens. Mater.* **23**, 455401.